NANO LETTERS

pubs.acs.org/NanoLett Letter

Nanopore Analysis of Malto-oligosaccharides from Amylose, Amylopectin, and Cyclodextrin Hydrolysates

Xinmeng Gao,[†] Yunqi Xiao,[†] Wenzheng Li, Lu Qian, Kefan Wang, Panke Zhang, and Shuo Huang*

Cite This: *Nano Lett.* 2026, 26, 74−82 Read Online

ACCESS | Metrics & More | Article Recommendations | Supporting Information

ABSTRACT: Malto-oligosaccharides, structurally diverse glucose polymers comprising 2−10 monosaccharide units, play vital roles in food science, pharmaceuticals, and glycobiology. However, their precise structural characterization remains challenging due to subtle chain-length variations and isomeric complexity that confound conventional analytical techniques. Here, we utilize a phenylboronic acid (PBA)-functionalized heterooctameric *Mycobacterium smegmatis* porin A nanopore (MspA-90PBA) to identify saccharides from glucose to maltooctaose. By simultaneous consideration of six event features via machine learning, a model was established and an over 98% validation accuracy was achieved. The method was validated using γ-cyclodextrin acidolysis products and subsequently applied to the differentiation of amylose and amylopectin, demonstrating its capability to discriminate between linear and branched polysaccharides. Finally, this technique was extended to the analysis of starch directly extracted from crop materials, confirming its robustness in real-world sample analysis.

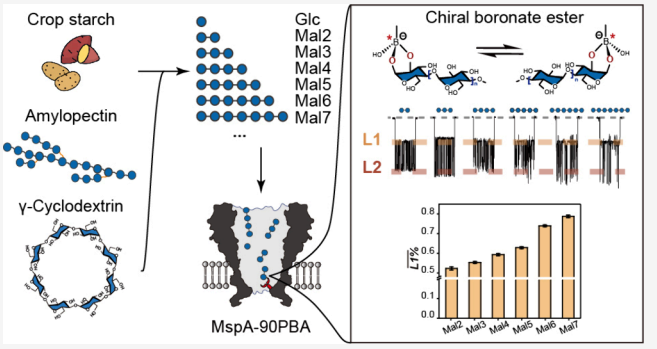

KEYWORDS: *malto-oligosaccharides, nanopore, machine learning, amylose, amylopectin, cyclodextrin*

Carbohydrates, one of the fundamental classes of biological molecules, exhibit structural diversity that far exceeds that of nucleic acids and proteins.[1−3] Oligosaccharides, consisting of 2−10 monosaccharide units, act as key building blocks of glycoconjugates,[4] molecules covalently linked to proteins[5] or lipids[6] via specific glycosidic bonds. These structures are integral components of the cell surface glycocalyx[7] and play pivotal roles in regulating intestinal microbiome dynamics[8] and modulating immune responses.[9] The complexity of oligosaccharides, arising from varied monosaccharide compositions,[10] diverse glycosidic linkages,[11] and branching heterogeneity, poses significant analytical challenges. Furthermore, their inherent instability to isomerization complicates high-purity sample preparation,[12] exacerbating analytical hurdles. Malto-oligosaccharides (MOSs),[13] linear glucose (Glc) polymers linked via α-1,4-glycosidic bonds, are widely found as hydrolysis products of starch.[14] Consequently, starchy crops such as corn, wheat, and sweet potatoes serve as primary raw materials for the production of MOSs.[15,16] Readily degradable by human digestive enzymes, MOSs are widely utilized in baked goods and sport beverages and as prebiotics to promote beneficial gut microbiota growth.[17]

Mass spectrometry (MS), nuclear magnetic resonance (NMR), and chromatographic methods currently represent the mainstream techniques for MOS analysis. MS enables the high-sensitivity determination of the degree of polymerization distribution[18] and glycosidic linkage characterization via fragment ion analysis.[19] However, it often requires complex derivatization procedures that may alter the native structures of MOSs.[20] Although NMR delivers precise stereochemical insights,[21] signal overlap in structurally similar molecules renders resonance assignment challenging.[22,23] Coupling hydrophilic interaction liquid chromatography with MS offers superior resolution yet requires time-intensive method optimization.[24,25] Consequently, rapid, label-free, accurate, and portable identification of different types of MOSs remains challenging.

Nanopore, a single-molecule analysis platform, has emerged as a powerful tool for nucleic acid sequencing,[26,27] protein detection,[28,29] and small-molecule sensing.[30−32] By confining analytes within a nanoscale aperture, this label-free approach enables real-time saccharide analysis without extensive sample pretreatment.[33,34] With biological nanopores, prior studies have utilized large protein adapters for saccharide sensing.[35,36] With solid-state nanopores, nanopore sensing of hyaluronic acid,[37,38] heparin,[39,40] and xylans[41] has been reported. Although nanopores have been applied to detect amylose

Received: September 12, 2025
Revised: December 13, 2025
Accepted: December 17, 2025
Published: December 31, 2025

https://doi.org/10.1021/acs.nanolett.5c04591
Nano Lett. 2026, 26, 74−82

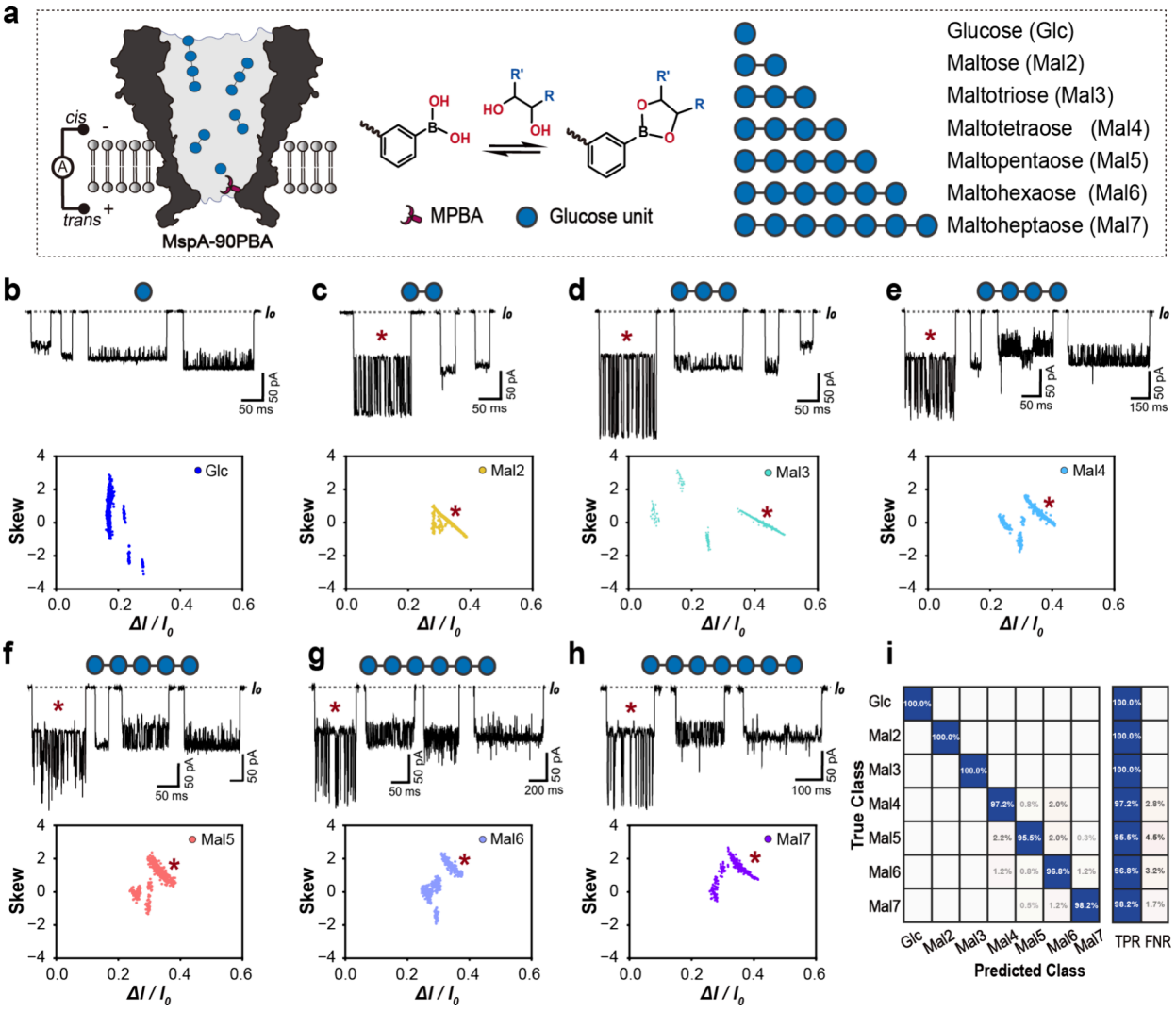

Figure 1. Identification of Glc and MOSs using MspA-90PBA. (a) Schematic diagram of Glc and six MOSs identification performed by MspA-90PBA via reversible boronate ester formation. The six MOSs, including maltose (Mal2), maltotriose (Mal3), maltotetraose (Mal4), maltopentaose (Mal5), maltohexaose (Mal6), and maltoheptaose (Mal7), consist of Glc units linked by α-1,4-glycosidic bonds. (b) Representative nanopore events and scatter plot of $\Delta I/I_o$ vs Skew recorded for Glc (n = 953). The I_o of MspA-90PBA is denoted by a gray dashed line. (c–h) Representative events and scatter plots of $\Delta I/I_o$ vs Skew values for Mal2 (n = 761, c), Mal3 (n = 739, d), Mal4 (n = 626, e), Mal5 (n = 650, f), Mal6 (n = 655, g), and Mal7 (n = 506, h) events, respectively. Data for each sample were obtained by acquiring results from three independent experiments. Asterisks denote characteristic signals in both raw events and scatter plots. (i) Six event features including $\Delta I/I_o$, SD, Skew, Max/I_o, Min/I_o, and IQR were extracted to construct a feature matrix (Figure S10). The confusion matrix was generated using a bagging tree model, achieving a validation accuracy of 98.2% (Figure S11 and Methods). Nanopore experiments were performed at a bias of +160 mV in 1.5 M KCl and 100 mM MOPS (pH 7.0) buffer. Each analyte was individually added to the *cis* chamber at 60 mM (Glc) or 20 mM (Mal2–Mal7).

(AM) and amylopectin (AP),[42,43] these efforts lacked monosaccharide resolution, precluding precise differentiation of chain-length variants. Consequently, systematic and high-resolution characterization of oligosaccharides by nanopores has remained challenging.

Previously, we developed a phenylboronic acid (PBA)-functionalized MspA nanopore (MspA-90PBA) that can discriminate nine monosaccharides[44] by leveraging reversible chemical interactions. This system further enabled the differentiation of glycosidic linkage configurations in disaccharides,[45] establishing a robust foundation for high-resolution oligosaccharide analysis. These results suggest the feasibility of direct nanopore identification of MOSs and other oligosaccharide fragments generated from the hydrolysis of starch, including AM, AP, or even starch directly extracted from crop materials.

Experimentally, a hetero-octameric *Mycobacterium smegmatis* porin A (MspA) nanopore composed of one N90C MspA-H6 subunit and seven M2MspA-D16H6 subunits was prepared and designated as $(N90C)_1(M2)_7$.[44] The cysteine residue at position 90 of a monomeric subunit was chemically modified with 3-(maleimide)phenylboronic acid (Methods). The resulting nanopore, bearing a single PBA adapter at position 90, is hereafter abbreviated as MspA-90PBA.

Due to the abundance of starch as source materials[15] and established production protocols, MOSs, α-1,4-linked Glc oligomers, can be synthesized in high yields to meet industrial demands. Commercial standard reagents, including Glc, maltose (Mal2), maltotriose (Mal3), maltotetraose (Mal4), maltopentaose (Mal5), maltohexaose (Mal6), and maltoheptaose (Mal7), were obtained and applied in nanopore measurements. These saccharides interact specifically with

https://doi.org/10.1021/acs.nanolett.5c04591
Nano Lett. 2026, 26, 74–82

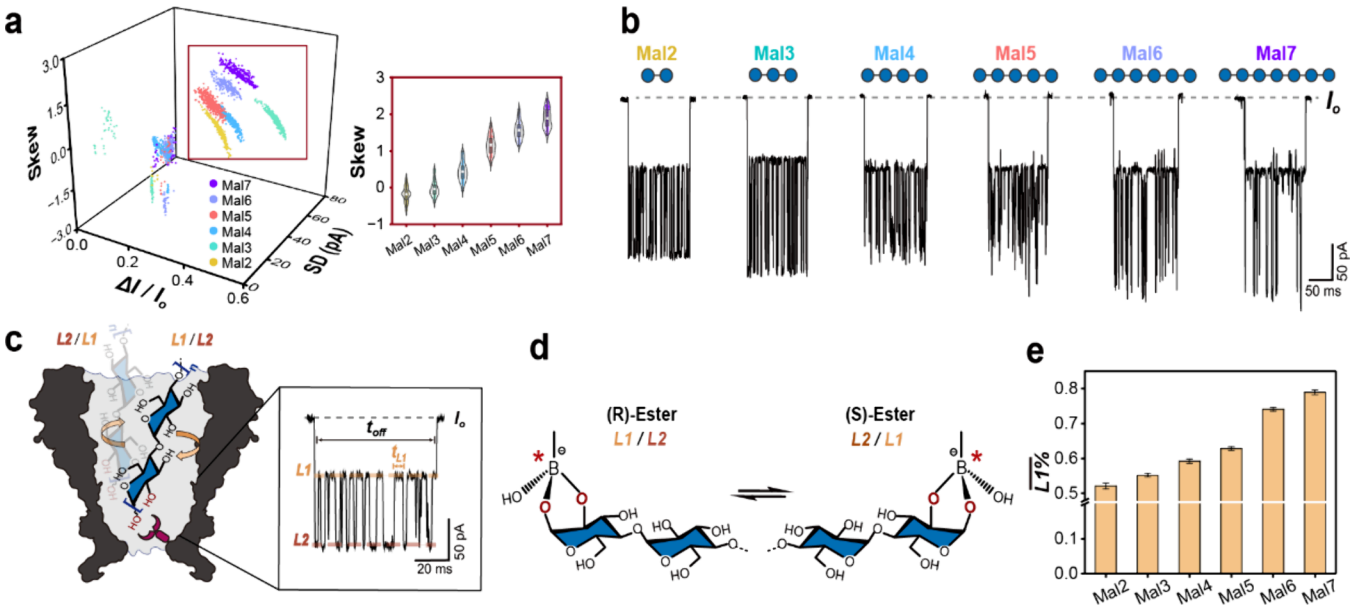

Figure 2. Characteristic events generated by the MOS. (a) 3D event scatter plot of results acquired with six MOSs, each comprising 400 events. The MOS characteristic events appear as clusters in regions with higher SD values, denoted by the red frame (Table S2 and Figure S15). The violin plot on the right illustrates the Skew feature variation across six MOSs. (b) Representative MOS characteristic events. (c) Level transition observed in the MOS characteristic events representing spontaneous switching between two molecular binding states (L1/L2) when captured by the nanopore. Here, t_{L1} corresponds to the duration of the L1 state, and t_{off} represents the event duration. (d) Switching between the L1 and L2 states in the event reflecting the inversion of chiral boronate ester (R/S configurations). (e) For each event, L1 %, calculated as L1 % $= \frac{\sum t_{L1}}{t_{off}}$. $\overline{\text{L1 \%}}$, was obtained by averaging L1 % values acquired with all events during each measurement. Generally, $\overline{\text{L1 \%}}$ increases with the number of Glc units from Mal2 to Mal7 (Table S5).

the PBA adapter via reversible boronate ester formation (Figure 1a), generating characteristic nanopore event features.

Nanopore measurements were conducted at an applied bias of +160 mV using 1.5 M KCl and 100 mM MOPS (pH 7.0) electrolyte buffer (Methods). The device chamber that is electrically grounded is defined as *cis*. Its opposing chamber is defined as *trans*. In separate measurements, all saccharides were added to the *cis* chamber at final concentrations of 20 mM for each MOS and 60 mM for Glc. Representative nanopore events for each saccharide are shown, with the open-pore current (I_o) of MspA-90PBA annotated by a gray dashed line. The plots of the current blockage ratio ($\Delta I/I_o$) and skewness (Skew) for Glc and MOSs (Mal2−Mal7) are presented in Figure 1b−h.

Events for each analyte were extracted from three independent measurements (Figures S1 and S2). Notably, each saccharide generated multiple event types, attributed to distinct binding configurations with the PBA adapter[46] and the high resolution of MspA-90PBA, which enabled discrimination of these different binding modes. Scatter plots and corresponding raw events highlighting these differences are provided in Figures S3−S9. Notably, all MOS (Mal2−Mal7) events exhibited a group of characteristic events, manifested as telegraphic switching signals, and are marked with asterisks in both raw traces and scatter plots. These events are tentatively designated here as characteristic events of MOS and will be discussed in subsequent sections.

From each event, six event features, including $\Delta I/I_o$, Skew, standard deviation (SD), maximum position of the signal current blockage ratio (Max/I_o), minimum position of the signal current blockage ratio (Min/I_o), and interquartile range (IQR), were extracted using MATLAB (Table S1 and Figure S10). A density-based spatial clustering of applications with noise (DBSCAN) algorithm was also employed to filter out noise events, which failed to form clear clusters. To further validate the discriminatory capability of MspA-90PBA for Glc and six MOSs, 500 data points randomly selected across all event types for each saccharide were used for machine learning (Methods). The bagging tree model yielded a confusion matrix with 98.2% validation accuracy (Figures 1i and S11) and is considered to be the optimum model. The trained model for Glc and MOS events is hereafter designated as the Glc-MOS model in subsequent discussions.

The limit of detection is defined as the minimum concentration at which at least two events could be detected within a 10 min continuous measurement (Table S3). Besides, the event appearance frequency ($1/\tau_{on}$) demonstrates a linear increase with the analyte concentration, which can be used for analyte quantification. The results of the concentration dependence measurements for different analytes are summarized in Table S4 and Figures S12−S14.

A 3D scatter plot of $\Delta I/I_o$ (X axis), SD (Y axis), and Skew (Z axis) was plotted (Figure 2a). For each type of MOS, a group of characteristic events manifested as clusters with high SD values (outlined by red boxes) were observed (Table S2 and Figure S15). Corresponding violin plot analysis of these characteristic events revealed a positive correlation between Skew and the number of Glc units (right panel, Figure 2a), indicating that the chain length influences signal characteristics. These characteristic MOS events (Figure 2b) consistently exhibited dual-level transitions, suggesting a consistent interaction mechanism among different oligomers. By classification of only these characteristic events using the six previously identified features (Figure S10), the SVM model

https://doi.org/10.1021/acs.nanolett.5c04591
Nano Lett. 2026, 26, 74−82

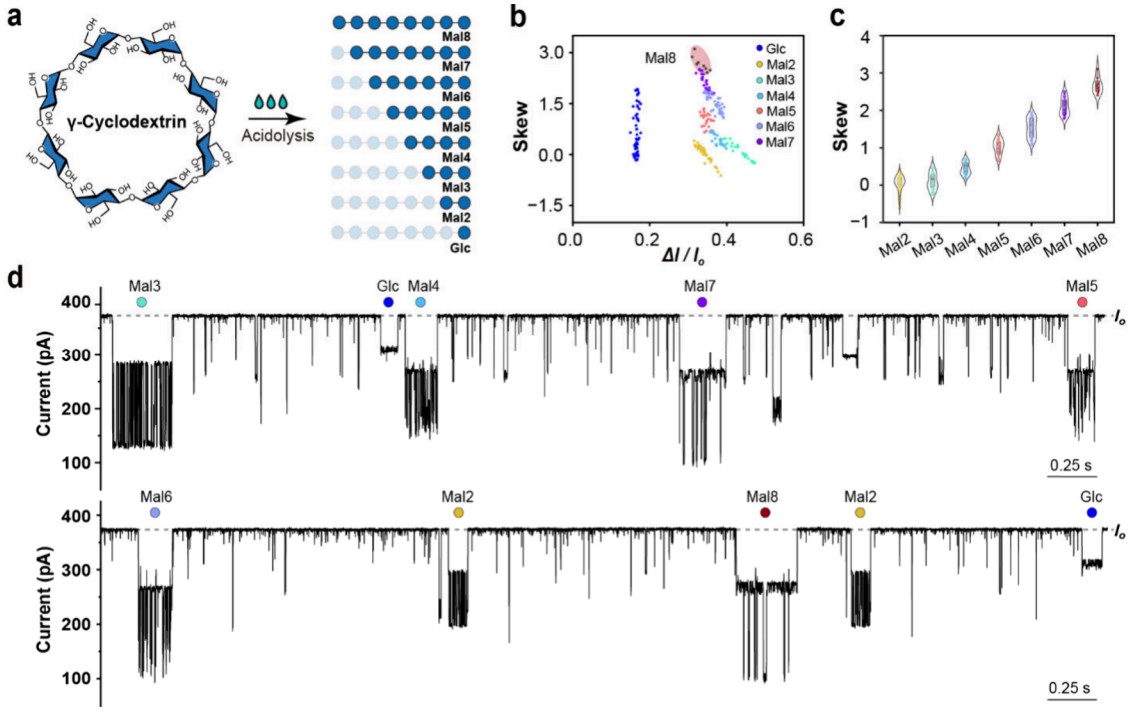

Figure 3. Nanopore analysis of acidolysis products of γ-CD. (a) Schematic illustration of γ-CD acidolysis. Glc, six MOSs, and the herein-reported maltooctaose (Mal8) are generated via the acid-catalyzed ring opening of γ-CD. (b) Event scatter plot of $\Delta I/I_o$ vs Skew (n = 258) from γ-CD acidolysis products. For the sake of clarity, only characteristic oligosaccharide signals (Figure 2b) are retained in the scatter plot (Figure S20). Newly recorded Mal8 events are highlighted by a red ellipse. (c) Violin plot depicting the distribution of Skew values for oligosaccharide events demonstrated in part b. (d) Representative trace acquired with the acidolysis products of γ-CD. Glc and all characteristic MOS events were labeled accordingly. The extremely short residing spiky events arise from undigested γ-CD (Figure S18).

achieved an accuracy of 99.7%, significantly outperforming models incorporating all event types (Figure S16). This result suggests that these characteristic events serve as a more reliable indicator of MOS identification.

To gain deeper insight into these characteristic signals, we further investigated their underlying chemical mechanism. Systematic studies on PBA−sugar polyol interactions could date back to 1949.[47] The stabilities of generated boronate esters generally follow the order furanose *cis*-1,2-diol > pyranose *cis*-1,2-diol > 1,3-diol ≫ *trans*-1,2-diol.[46,48,49] The *cis*-1,2-diol at the reducing end of maltose has been shown to exhibit a higher binding affinity to PBA[50] and may be the cause of the long-residing, characteristic events of MOS. To confirm this structural mechanism, *p*-nitrophenyl-β-D-maltoside, which lacks the hemiacetal hydroxyl group necessary for forming a *cis*-1,2-diol at the reducing end, was used as a negative control analyte. Experimentally, with *p*-nitrophenyl-β-D-maltoside, the previously observed characteristic events disappeared, and only extremely short residing events were shown instead (Figure S17), confirming that the characteristic MOS events originate from boronate ester formation between the *cis*-1,2-diol at the reducing end and the PBA adapter.

Based on the structure of MspA-90PBA and boronate ester binding dynamics, a schematic using Mal2 as a representative analyte was constructed (Figure 2c). Each event displayed two distinct blockage levels: L1 (light orange, upper blockage level) and L2 (dark orange, lower blockage level). As previously reported, phenylboronate esters undergo chiral interconversion between *R*/*S* configurations within the confined nanopore environment.[51] Here, the reducing end of the MOS forms a boronate ester with the PBA adapter, and its dynamic *R*/*S* chirality generates two binding states (L1/L2, Figure 2d). For each event, the temporal ratio of the L1 state (L1 %) was calculated as L1 % = $(\sum t_{L1})/t_{off}$. Analysis of the mean temporal ratio of L1 % ($\overline{\text{L1 \%}}$) revealed a positive correlation with the chain length of MOS (Figure 2e and Table S5), indicating that steric hindrance progressively restricts deep binding (L2) in longer oligosaccharides. This mechanistic insight explains the systematic increase in Skew values with Glc unit addition (right panel, Figure 2a). While the exact mapping between *R*/*S* configurations and L1/L2 states requires future computational simulation, this work establishes the preliminary mechanistic explanation of this phenomenon.

Having established the analytical framework for MOS characterization (Mal2−Mal7), we extended this methodology to the analysis of γ-cyclodextrin (γ-CD). We utilized γ-CD, a cyclic octasaccharide composed of α-1,4-linked Glc units formed via CGTase-mediated starch cyclization,[52] as a well-defined model substrate. Direct nanopore sensing of untreated γ-CD generated only short-residing spiky events (Figure S18), indicating no specific interaction with the MspA-90PBA nanopore. To produce linear oligomers, γ-CD was subjected to acidolysis using 3 M HCl followed by pH neutralization and ultrafiltration (Methods). Afterward, 75 μL of the acidolysis filtrate was introduced to the *cis* chamber to initiate nanopore analysis.

Acid hydrolysis randomly cleaves α-1,4-glycosidic bonds in γ-CD, generating a mixture of Glc and MOS species ranging from Mal2 to Mal8 (Figure 3a). One-Class Support Vector Machine (OC-SVM), a machine learning algorithm specialized in outlier detection, was employed to characterize the composition of γ-CD acidolysis products (Methods). Using

https://doi.org/10.1021/acs.nanolett.5c04591
Nano Lett. 2026, 26, 74−82

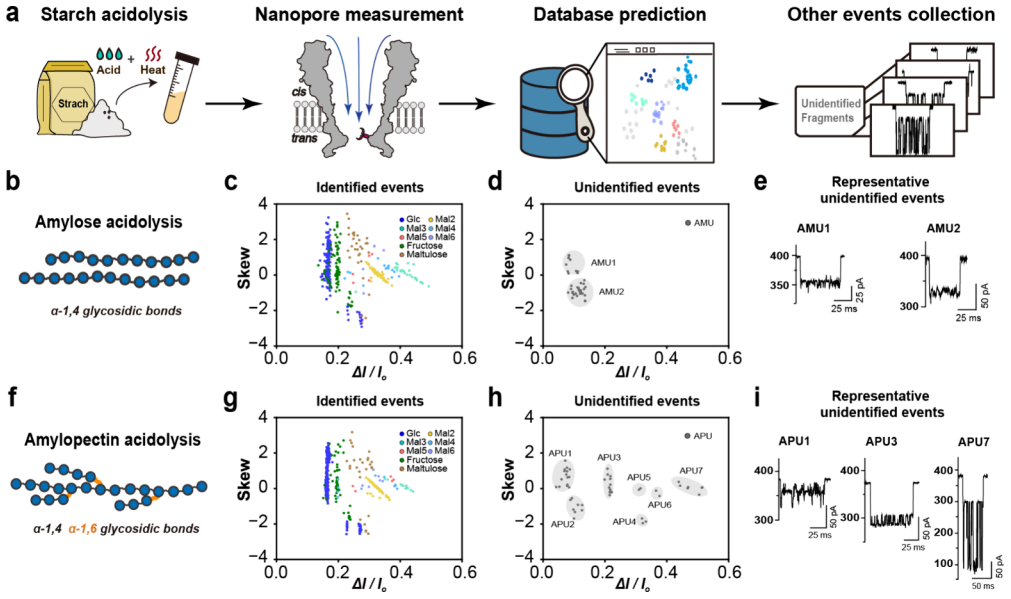

Figure 4. Nanopore analysis of thermal acidolysis products of AM and AP. (a) Workflow for nanopore characterization of acidolysis products of AM and AP. Following thermal acidolysis (Methods) and nanopore analysis, the generated saccharide events were divided into inlier and outlier events based on the results of OC-SVM analysis using the same data as the Glc-MOS-FM model (Methods and Figures S23−S24). The outlier events were designated as AM or AP unidentified events, respectively. (b) Schematic of AM (linear α-1,4-linked Glc chains). (c) Event scatter plot of $\Delta I/I_o$ vs Skew (n = 451) for identified events acquired with AM acidolysis products. (d) Event scatter plot of $\Delta I/I_o$ vs Skew (n = 36) for unidentified events acquired with AM acidolysis products, abbreviated as "AMU" (Figure S25). Distinct types of events were labeled as AMU1 and -2. (e) Representative events of the AMU. (f) Schematic of AP (α-1,4-linked chains with α-1,6-branch points, orange). (g) Event scatter plot of $\Delta I/I_o$ vs Skew (n = 535) for identified events acquired with AP acidolysis products. (h) Event scatter plot of $\Delta I/I_o$ vs Skew (n = 52) for unidentified events acquired with AP acidolysis products, abbreviated as "APU" (Figure S26). These events were labeled as APU1−7. (i) Representative events of APU (additional types are shown in Figure S29).

the same data set previously used to establish the Glc-MOS classification model, all raw events were categorized into "inliers" and "outliers" (Figure S19). According to predictions by the Glc-MOS model, the inlier events were classified as Glc or six types of MOS (Mal2−Mal7). A previously uncharacterized cluster of events, considered an outlier cluster, was also reported. Considering γ-CD's inherent octasaccharide structure, this cluster likely corresponds to the maltooctaose (Mal8) events. Violin plot analysis of these events revealed a systematic increase in Skew values (Figure 3c) and a consistent ($\overline{\text{L1 \%}}$) trend with shorter MOS chains (Figure S21), supporting that the uncharacterized cluster was generated by Mal8. All noncharacteristic MOS events were excluded for analysis (Figure S20), and the resulting scatter plot (Figure 3b) displays events of Glc and only characteristic MOS events, with Mal8 events highlighted by a red ellipse.

A representative trace acquired with γ-CD acidolysis products is shown in Figure 3d. Short residing spiky events should correspond to nonspecific collisions of undigested γ-CD (Figure S18). Glc and characteristic MOS events are marked with the corresponding color-coded dots. For the sake of clarity, all other MOS events are unlabeled. These results demonstrate the capacity of MspA-90PBA to achieve high-resolution discrimination of Glc and seven MOSs (Mal2−Mal8), suggesting its potential for characterizing complex glycan mixtures in industrial and biomedical applications.

The insights gained from the above results inspired us to investigate more complex starch systems. Starch, a high-molecular-weight Glc polymer, consists of two structurally distinct components: amylose (AM) and amylopectin (AP).[53] Specifically, AM comprises linear α-1,4-linked Glc chains (Figure 4b), whereas AP exhibits a branched architecture with α-1,6 linkages at branching points (Figure 4f). The initial nanopore analysis of untreated AM and AP water suspensions (0.7 mg/mL) revealed sporadic current blockages with irregular amplitudes (Figure S22). These phenomena can likely be attributed to the structural polydispersity and heterogeneous aggregation of native starch. While direct nanopore analysis revealed minor differences between AM and AP, the current data restricted reliable acquisition of meaningful information.

To obtain more interpretable results, thermal acidolysis was performed on AM and AP to generate the corresponding oligomeric fragments (Figure 4a and Methods). For nanopore measurements, 50 μL aliquots of ultrafiltered AM and AP acidolysis products were separately introduced to the *cis* chamber. From visual inspection, events corresponding to fructose and maltulose were also detected. To enable machine-learning-based event identification, the training data of fructose and maltulose were integrated into the Glc-MOS classification data set. Using this updated data set, the bagging tree algorithm attained a 98.1% validation accuracy. The resulting expanded model, named Glc-MOS-FM, was subsequently applied to analyze AM and AP thermal acidolysis products (Figure S23). Using this updated data set and the OC-SVM algorithm, nanopore events were partitioned into inlier and outlier populations (Figure S24 and Methods). Predicted by the Glc-MOS-FM model, all inlier events were further classified as Glc, MOS, fructose, and maltulose, and the results are shown in Figure 4c,g. Possibly due to nonspecific degradation and suboptimal experimental conditions, MOSs larger than Mal6 were not seen. Instead, all outlier events, respectively generated from AM and AP, were tentatively designated as "AM unidentified" (AMU) and "AP unidenti-

https://doi.org/10.1021/acs.nanolett.5c04591
Nano Lett. 2026, 26, 74−82

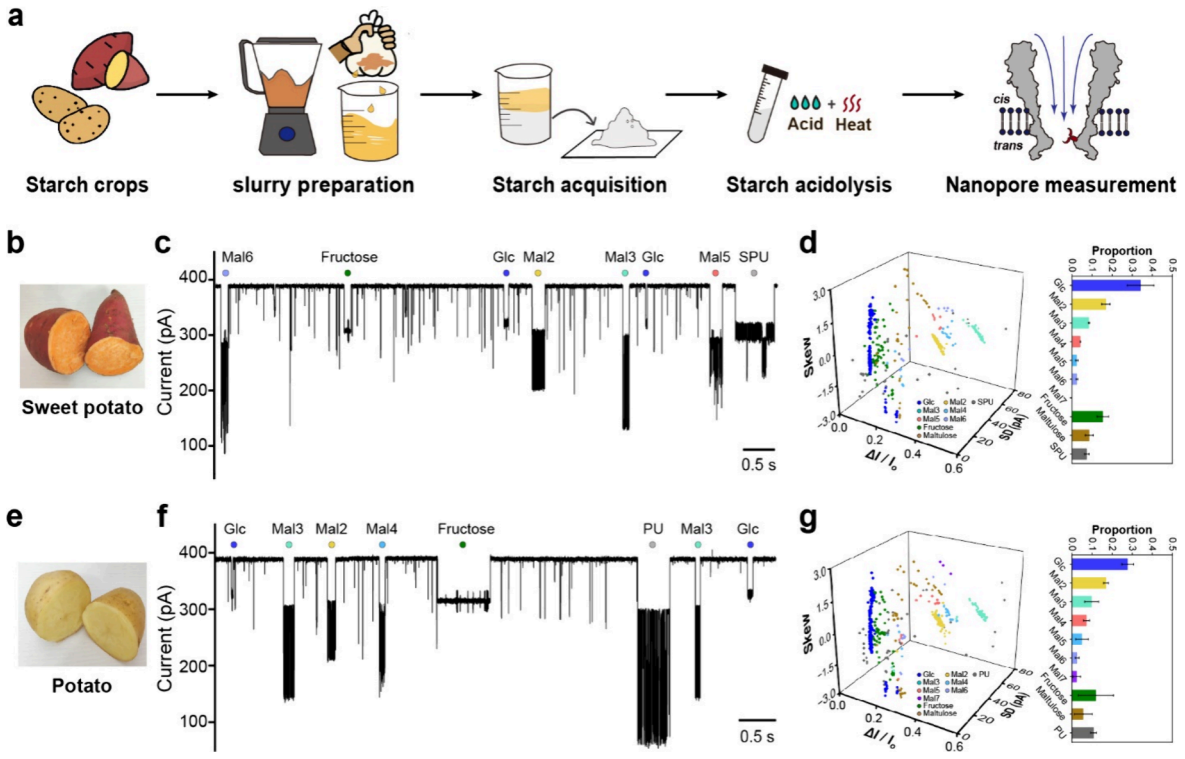

Figure 5. Nanopore analysis of MOSs from crop starch hydrolysates. (a) The workflow. Sweet potato and potato were homogenized, filtered, and sedimented to obtain starch, respectively (Figure S35). The extracted starch was subjected to thermal acidolysis (Methods), and the resulting fragments were analyzed using the MspA-90PBA nanopore. (b) Sweet potato. (c) Representative trace acquired with sweet potato starch hydrolysates. (d) 3D event scatter plot ($\Delta I/I_o$, SD, and Skew) of results obtained with sweet potato hydrolysates (n = 456). Events were classified and color-coded using the established Glc-MOS-FM model (Figure S36 and Methods). The relative proportions are shown on the right calculated from event counts. Error bars represent the mean ± SD derived from the results of three independent trials (Figure S37). (e) Potato. (f) Representative trace acquired with potato starch hydrolysates. (g) 3D event scatter plot of results obtained with potato hydrolysates (n = 450), with the relative proportions shown on the right (Figure S38).

fied" (APU) events. AMU and APU events are shown separately in Figure 4d,h, where distinct event clusters are labeled as AMU1 and -2 and APU1−7, respectively.

To show the result consistency, with AM and AP thermal acidolysis products, results of three independent measurements are presented in Figures S25 and S26, with corresponding representative traces shown in Figures S27 and S28. Generally, APU exhibits more event clusters than AMU, likely attributable to the complex branched architecture of AP. However, due to a lack of well-characterized standard analytes, the exact structures corresponding to these events could not be fully determined. Representative events of AMU and APU are shown in Figure 4e,i. Additional subtypes of unidentified events are displayed in Figure S29.

Nanopore events of fructose and maltulose,[44,45] along with representative events from acidolysis products, are presented in Figures S30 and S31. Because AM and AP are composed of Glc monomeric units, the presence of fructose and maltulose was unexpected. Previous studies have shown that Glc could undergo thermal isomerization to fructose via chemical catalysis,[54−56] while maltulose may arise from heat-induced isomerization of maltose,[57,58] explaining the presence of fructose and maltulose in this assay. These pathways were confirmed by separate thermal experiments (Figures S32−S33), demonstrating that the applied acidolysis conditions inadvertently induced isomerization side reactions. Collectively, these results demonstrate the utility of MspA-90PBA as a robust analytical tool capable of revealing subtle molecular details in complex biological samples.

To further verify the robustness and specificity of MspA-90PBA in the presence of interferences, chitosan oligosaccharide, composed of glucosamine units linked by β-1,4-glycosidic bonds and lacking *cis*-1,2-diols, was measured. However, only occasional transient spiky events were detected. When chitosan oligosaccharide was mixed with maltose and subjected to measurement, the maltose events remained clearly distinguishable (Figure S34).

This technique was further extended to the analysis of starch extracted from crop materials. Starch was first isolated from sweet potatoes and potatoes through slurry preparation, sedimentation, and drying (Figure S35), followed by the same thermal acidolysis protocol employed for commercial AM and AP samples (Figure 5a and Methods). A total of 50 μL of the ultrafiltered acidolysis products was loaded into the *cis* chamber to initiate the measurement.

The resulting hydrolysates were directly analyzed using MspA-90PBA, and the data were processed via the OC-SVM workflow and the established Glc-MOS-FM classification model (Figure S36). Representative traces obtained from sweet potato (Figure 5c) and potato starch hydrolysates (Figure 5f) exhibited complex event mixtures. Assisted by machine learning, Glc, MOSs (Mal2−Mal6 for sweet potato and Mal2−Mal7 for potato), fructose, and maltulose were clearly identified. The unidentified events, designated as "SPU" (Sweet Potato Unidentified) and "PU" (Potato Unidentified),

https://doi.org/10.1021/acs.nanolett.5c04591
Nano Lett. 2026, 26, 74−82

demonstrated that sample-specific fragments were respectively detected. Three-dimensional (3D) event scatter plots of $\Delta I/I_o$, SD, and Skew clearly displayed distinct clusters corresponding to the hydrolysis products of sweet potato and potato starch (Figure 5d,g). The relative event proportions on the right serve as characteristic fingerprints for these hydrolysates. Data from three independent measurements are also presented in Figures S37−S38. These findings collectively underscore the potential utility of nanopores in food chemistry and glycomic analysis.

In summary, MspA-90PBA enabled the simultaneous identification of Glc and a series of MOSs, including maltose (Mal2), maltotriose (Mal3), maltotetraose (Mal4), maltopentaose (Mal5), maltohexaose (Mal6), maltoheptaose (Mal7), and maltooctaose (Mal8), with each analyte exhibiting distinct event features. By the integration of six event features via machine learning, a 98.2% validation accuracy was achieved. Each MOS type displayed a characteristic event group, originating from PBA−*cis*-1,2-diol interaction at the reducing end. This sensing strategy was validated in the analysis of γ-CD acidolysis products. Subsequent nanopore analysis of AM and AP hydrolysates revealed distinct event cluster distributions, demonstrating their ability to discriminate between linear and branched polysaccharides. Additional events from heat-induced isomerization products, such as fructose and maltulose, were also identified. Finally, the platform was extended to starch directly extracted from crop materials, which yielded sample-specific hydrolysate profiles. This method offers a direct, rapid, portable, label-free, and high-resolution approach for analyzing naturally obtained oligosaccharides, paving the way for nanopore glycan sequencing.

■ ASSOCIATED CONTENT

Supporting Information

The Supporting Information is available free of charge at https://pubs.acs.org/doi/10.1021/acs.nanolett.5c04591.

Materials, detailed methods for nanopore experiments and sample preparation, tables of key parameters for Glc and MOS, figures of nanopore events, representative current traces, machine learning, and data processing (PDF)

■ AUTHOR INFORMATION

Corresponding Author

Shuo Huang − *State Key Laboratory of Analytical Chemistry for Life Sciences, School of Chemistry and Chemical Engineering and Chemistry and Biomedicine Innovation Center (ChemBIC), Nanjing University, Nanjing 210023, China;* orcid.org/0000-0001-6133-7027; Email: shuo.huang@nju.edu.cn

Authors

Xinmeng Gao − *State Key Laboratory of Analytical Chemistry for Life Sciences, School of Chemistry and Chemical Engineering and Chemistry and Biomedicine Innovation Center (ChemBIC), Nanjing University, Nanjing 210023, China*

Yunqi Xiao − *State Key Laboratory of Analytical Chemistry for Life Sciences, School of Chemistry and Chemical Engineering and Chemistry and Biomedicine Innovation Center (ChemBIC), Nanjing University, Nanjing 210023, China*

Wenzheng Li − *State Key Laboratory of Analytical Chemistry for Life Sciences, School of Chemistry and Chemical Engineering and Chemistry and Biomedicine Innovation Center (ChemBIC), Nanjing University, Nanjing 210023, China*

Lu Qian − *State Key Laboratory of Analytical Chemistry for Life Sciences, School of Chemistry and Chemical Engineering and Chemistry and Biomedicine Innovation Center (ChemBIC), Nanjing University, Nanjing 210023, China*

Kefan Wang − *State Key Laboratory of Analytical Chemistry for Life Sciences, School of Chemistry and Chemical Engineering and Chemistry and Biomedicine Innovation Center (ChemBIC), Nanjing University, Nanjing 210023, China*

Panke Zhang − *State Key Laboratory of Analytical Chemistry for Life Sciences, School of Chemistry and Chemical Engineering, Nanjing University, Nanjing 210023, China;* orcid.org/0000-0001-8562-9972

Complete contact information is available at: https://pubs.acs.org/10.1021/acs.nanolett.5c04591

Author Contributions

†X.G. and Y.X. contributed equally to this work. S.H. and X.G. conceived the project. X.G. prepared the MspA nanopores. X.G., W.L., and L.Q. performed the measurements. X.G. and Y.X. designed the machine-learning algorithms. P.Z. set up the instruments. S.H. and X.G. wrote the paper. S.H. and K.W. supervised the project.

Funding

The National Key R&D Program of China (Grant 2022YFA1304602), National Natural Science Foundation of China (Grants 22225405 and 22534004), the Fundamental Research Funds for the Central Universities (Grant 020514380336), State Key Laboratory of Analytical Chemistry for Life Science (Grant 5431ZZXM2509), National Natural Science Foundation of China (Grant 223B2402 to K.F.W.), China National Postdoctoral Program for Innovative Talents (Grant BX20250087 to K.F.W.), Jiangsu Funding Program for Excellent Postdoctoral Talent (Grant 2025ZB212 to K.F.W.), and Yachen Foundation of Nanjing University provided financial support.

Notes

The authors declare the following competing financial interest(s): S.H. has filed patents describing the preparation of heterogeneous MspA and its applications.

■ REFERENCES

(1) Cao, L.; Wang, L. Biospecific Chemistry for Covalent Linking of Biomacromolecules. *Chem. Rev.* **2024**, *124* (13), 8516−8549.
(2) Fontana, C.; Widmalm, G. Primary Structure of Glycans by NMR Spectroscopy. *Chem. Rev.* **2023**, *123* (3), 1040−1102.
(3) Tommasone, S.; Allabush, F.; Tagger, Y. K.; Norman, J.; Köpf, M.; Tucker, J. H. R.; Mendes, P. M. The challenges of glycan recognition with natural and artificial receptors. *Chem. Soc. Rev.* **2019**, *48* (22), 5488−5505.
(4) Crawford, C. J.; Seeberger, P. H. Advances in glycoside and oligosaccharide synthesis. *Chem. Soc. Rev.* **2023**, *52* (22), 7773−7801.
(5) Tsai, Y.-X.; Chang, N.-E.; Reuter, K.; Chang, H.-T.; Yang, T.-J.; von Bülow, S.; Sehrawat, V.; Zerrouki, N.; Tuffery, M.; Gecht, M. Rapid simulation of glycoprotein structures by grafting and steric exclusion of glycan conformer libraries. *Cell* **2024**, *187* (5), 1296−1311.

(6) Liu, X.; Dong, T.; Zhou, Y.; Huang, N.; Lei, X. Exploring the Binding Proteins of Glycolipids with Bifunctional Chemical Probes. *Angew. Chem., Int. Ed.* **2016**, *55* (46), 14330−14334.
(7) Bussin, B.; MacDuff, M. G. G.; Ngo, W.; Chan, W. C. W. Cellular Glycocalyx Affects Nanoparticle Access to Cell Membranes and Uptake. *Adv. Mater.* **2025**, *37*, No. e2503004.
(8) Luis, A. S.; Hansson, G. C. Intestinal mucus and their glycans: A habitat for thriving microbiota. *Cell Host Microbe* **2023**, *31* (7), 1087−1100.
(9) Pinho, S. S.; Alves, I.; Gaifem, J.; Rabinovich, G. A. Immune regulatory networks coordinated by glycans and glycan-binding proteins in autoimmunity and infection. *Cell. Mol. Immunol.* **2023**, *20* (10), 1101−1113.
(10) Liu, D.; Tang, W.; Yin, J.-Y.; Nie, S.-P.; Xie, M.-Y. Monosaccharide composition analysis of polysaccharides from natural sources: Hydrolysis condition and detection method development. *Food Hydrocoll.* **2021**, *116*, No. 106641.
(11) de Haan, N.; Yang, S.; Cipollo, J.; Wuhrer, M. Glycomics studies using sialic acid derivatization and mass spectrometry. *Nat. Rev. Chem.* **2020**, *4* (5), 229−242.
(12) Zhang, H.; Luo, J.; Liu, L.; Chen, X.; Wan, Y. Green production of sugar by membrane technology: How far is it from industrialization? *Green Chem. Eng.* **2021**, *2* (1), 27−43.
(13) Bláhová, M.; Štefuca, V.; Hronská, H.; Rosenberg, M. Maltooligosaccharides: Properties, Production and Applications. *Molecules* **2023**, *28* (7), 3281.
(14) Wang, Y.; Bai, Y.; Ji, H.; Dong, J.; Li, X.; Liu, J.; Jin, Z. Insights into rice starch degradation by maltogenic α−amylase: Effect of starch structure on its rheological properties. *Food Hydrocoll.* **2022**, *124*, No. 107289.
(15) Waterschoot, J.; Gomand, S. V.; Fierens, E.; Delcour, J. A. Production, structure, physicochemical and functional properties of maize, cassava, wheat, potato and rice starches. *Starch* **2015**, *67* (1−2), 14−29.
(16) Ye, F.; Li, J.; Zhao, G. Physicochemical properties of different-sized fractions of sweet potato starch and their contributions to the quality of sweet potato starch. *Food Hydrocoll.* **2020**, *108*, No. 106023.
(17) Cheng, W.; Lu, J.; Li, B.; Lin, W.; Zhang, Z.; Wei, X.; Sun, C.; Chi, M.; Bi, W.; Yang, B.et al.Effect of Functional Oligosaccharides and Ordinary Dietary Fiber on Intestinal Microbiota Diversity. *Front. Microbiol.* **2017**, *8*. DOI: 10.3389/fmicb.2017.01750.
(18) Qu, L.; Jiang, Y.; Huang, X.; Cui, M.; Ning, F.; Liu, T.; Gao, Y.; Wu, D.; Nie, Z.; Luo, L. High-Throughput Monitoring of Multiclass Syrup Adulterants in Honey Based on the Oligosaccharide and Polysaccharide Profiles by MALDI Mass Spectrometry. *J. Agric. Food Chem.* **2019**, *67* (40), 11256−11261.
(19) Yang, Q.; Guo, Y.; Jiang, Y.; Yang, B. Structure identification of the oligosaccharides by UPLC-MS/MS. *Food Hydrocoll.* **2023**, *139*, No. 108558.
(20) Wang, J.; Zhao, J.; Nie, S.; Xie, M.; Li, S. MALDI mass spectrometry in food carbohydrates analysis: A review of recent researches. *Food Chem.* **2023**, *399*, No. 133968.
(21) Yao, H.-Y.-Y.; Wang, J.-Q.; Yin, J.-Y.; Nie, S.-P.; Xie, M.-Y. A review of NMR analysis in polysaccharide structure and conformation: Progress, challenge and perspective. *Food Res. Int.* **2021**, *143*, No. 110290.
(22) Zhang, H.; Zhang, N.; Xiong, Z.; Wang, G.; Xia, Y.; Lai, P.; Ai, L. Structural characterization and rheological properties of β-D-glucan from hull-less barley (Hordeum vulgare L. var. nudum Hook. f.). *Phytochemistry* **2018**, *155*, 155−163.
(23) Gray, C. J.; Migas, L. G.; Barran, P. E.; Pagel, K.; Seeberger, P. H.; Eyers, C. E.; Boons, G.-J.; Pohl, N. L. B.; Compagnon, I.; Widmalm, G. Advancing Solutions to the Carbohydrate Sequencing Challenge. *J. Am. Chem. Soc.* **2019**, *141* (37), 14463−14479.
(24) Juvonen, M.; Kotiranta, M.; Jokela, J.; Tuomainen, P.; Tenkanen, M. Identification and structural analysis of cereal arabinoxylan-derived oligosaccharides by negative ionization HILIC-MS/MS. *Food Chem.* **2019**, *275*, 176−185.
(25) Xiao, Z.; Hou, X.; Zhang, T.; Yuan, Y.; Xiao, J.; Song, W.; Yue, T. Starch-digesting product analysis based on the hydrophilic interaction liquid chromatography coupled mass spectrometry method to evaluate the inhibition of flavonoids on pancreatic α-amylase. *Food Chem.* **2022**, *372*, No. 131175.
(26) Ayub, M.; Hardwick, S. W.; Luisi, B. F.; Bayley, H. Nanopore-Based Identification of Individual Nucleotides for Direct RNA Sequencing. *Nano Lett.* **2013**, *13* (12), 6144−6150.
(27) Manrao, E. A.; Derrington, I. M.; Laszlo, A. H.; Langford, K. W.; Hopper, M. K.; Gillgren, N.; Pavlenok, M.; Niederweis, M.; Gundlach, J. H. Reading DNA at single-nucleotide resolution with a mutant MspA nanopore and phi29 DNA polymerase. *Nat. Biotechnol.* **2012**, *30* (4), 349−353.
(28) Liu, Y.; Wang, K.; Wang, Y.; Wang, L.; Yan, S.; Du, X.; Zhang, P.; Chen, H.-Y.; Huang, S. Machine Learning Assisted Simultaneous Structural Profiling of Differently Charged Proteins in a Mycobacterium smegmatis Porin A (MspA) Electroosmotic Trap. *J. Am. Chem. Soc.* **2022**, *144* (2), 757−768.
(29) Horne, R. I.; Sandler, S. E.; Vendruscolo, M.; Keyser, U. F. Detection of protein oligomers with nanopores. *Nat. Rev. Chem.* **2025**, *9* (4), 224−240.
(30) Chingarande, R. G.; Tian, K.; Kuang, Y.; Sarangee, A.; Hou, C.; Ma, E.; Ren, J.; Hawkins, S.; Kim, J.; Adelstein, R. Real-time label-free detection of dynamic aptamer−small molecule interactions using a nanopore nucleic acid conformational sensor. *Proc. Natl. Acad. Sci. U. S. A.* **2023**, *120* (24), No. e2108118120.
(31) Sun, W.; Xiao, Y.; Wang, K.; Zhang, S.; Yao, L.; Li, T.; Cheng, B.; Zhang, P.; Huang, S. Nanopore discrimination of rare earth elements. *Nat. Nanotechnol.* **2025**, *20* (4), 523−531.
(32) Wang, K.; Zhang, S.; Zhou, X.; Yang, X.; Li, X.; Wang, Y.; Fan, P.; Xiao, Y.; Sun, W.; Zhang, P. Unambiguous discrimination of all 20 proteinogenic amino acids and their modifications by nanopore. *Nat. Methods* **2024**, *21* (1), 92−101.
(33) Ramsay, W. J.; Bayley, H. Single-Molecule Determination of the Isomers of d-Glucose and d-Fructose that Bind to Boronic Acids. *Angew. Chem., Int. Ed.* **2018**, *57* (11), 2841−2845.
(34) Bayat, P.; Rambaud, C.; Priem, B.; Bourderioux, M.; Bilong, M.; Poyer, S.; Pastoriza-Gallego, M.; Oukhaled, A.; Mathé, J.; Daniel, R. Comprehensive structural assignment of glycosaminoglycan oligo- and polysaccharides by protein nanopore. *Nat. Commun.* **2022**, *13* (1), 5113.
(35) Li, X.; Lee, K. H.; Shorkey, S.; Chen, J.; Chen, M. Different Anomeric Sugar Bound States of Maltose Binding Protein Resolved by a Cytolysin A Nanopore Tweezer. *ACS Nano* **2020**, *14* (2), 1727−1737.
(36) Galenkamp, N. S.; Soskine, M.; Hermans, J.; Wloka, C.; Maglia, G. Direct electrical quantification of glucose and asparagine from bodily fluids using nanopores. *Nat. Commun.* **2018**, *9* (1), 4085.
(37) Rivas, F.; Zahid, O. K.; Reesink, H. L.; Peal, B. T.; Nixon, A. J.; DeAngelis, P. L.; Skardal, A.; Rahbar, E.; Hall, A. R. Label-free analysis of physiological hyaluronan size distribution with a solid-state nanopore sensor. *Nat. Commun.* **2018**, *9* (1), 1037.
(38) Rivas, F.; DeAngelis, P. L.; Rahbar, E.; Hall, A. R. Optimizing the sensitivity and resolution of hyaluronan analysis with solid-state nanopores. *Sci. Rep.* **2022**, *12* (1), 4469.
(39) Karawdeniya, B. I.; Bandara, Y. M. N. D. Y.; Nichols, J. W.; Chevalier, R. B.; Dwyer, J. R. Surveying silicon nitride nanopores for glycomics and heparin quality assurance. *Nat. Commun.* **2018**, *9* (1), 3278.
(40) Xia, K.; Hagan, J. T.; Fu, L.; Sheetz, B. S.; Bhattacharya, S.; Zhang, F.; Dwyer, J. R.; Linhardt, R. J. Synthetic heparan sulfate standards and machine learning facilitate the development of solid-state nanopore analysis. *Proc. Natl. Acad. Sci. U. S. A.* **2021**, *118* (11), No. e2022806118.
(41) Cai, Y.; Zhang, B.; Liang, L.; Wang, S.; Zhang, L.; Wang, L.; Cui, H.-L.; Zhou, Y.; Wang, D. A solid-state nanopore-based single-molecule approach for label-free characterization of plant polysaccharides. *Plant Communications* **2021**, *2* (2), 100106.

https://doi.org/10.1021/acs.nanolett.5c04591
Nano Lett. 2026, 26, 74−82

(42) Bacri, L.; Oukhaled, A.; Hémon, E.; Bassafoula, F. B.; Auvray, L.; Daniel, R. Discrimination of neutral oligosaccharides through a nanopore. *Biochem. Biophys. Res. Commun.* **2011**, *412* (4), 561−564.
(43) Xie, W.; He, S.; Fang, S.; Yin, B.; Tian, R.; Wang, Y.; Wang, D. Analysis of starch dissolved in ionic liquid by glass nanopore at single molecular level. *Int. J. Biol. Macromol.* **2023**, *239*, No. 124271.
(44) Zhang, S.; Cao, Z.; Fan, P.; Wang, Y.; Jia, W.; Wang, L.; Wang, K.; Liu, Y.; Du, X.; Hu, C. A Nanopore-Based Saccharide Sensor. *Angew. Chem., Int. Ed.* **2022**, *61* (33), No. e202203769.
(45) Zhang, S.; Cao, Z.; Fan, P.; Sun, W.; Xiao, Y.; Zhang, P.; Wang, Y.; Huang, S. Discrimination of Disaccharide Isomers of Different Glycosidic Linkages Using a Modified MspA Nanopore. *Angew. Chem., Int. Ed.* **2024**, *63* (8), No. e202316766.
(46) Miyazaki, Y.; Fujimori, T.; Okita, H.; Hirano, T.; Yoshimura, K. Thermodynamics of complexation reactions of borate and phenylboronate with diol, triol and tetritol. *Dalton Trans.* **2013**, *42* (29), 10473−10486.
(47) Böeseken, J. The Use of Boric Acid for the Determination of the Configuration of Carbohydrates. *Advances in Carbohydrate Chemistry*; Academic Press, 1949; Vol. *4*, pp 189−210. DOI: 10.1016/S0096-5332(08)60049-1.
(48) Peters, J. A. Interactions between boric acid derivatives and saccharides in aqueous media: Structures and stabilities of resulting esters. *Coord. Chem. Rev.* **2014**, *268*, 1−22.
(49) Brooks, W. L. A.; Deng, C. C.; Sumerlin, B. S. Structure−Reactivity Relationships in Boronic Acid−Diol Complexation. *ACS Omega* **2018**, *3* (12), 17863−17870.
(50) van den Berg, R.; Peters, J. A.; van Bekkum, H. The structure and (local) stability constants of borate esters of mono- and disaccharides as studied by 11B and 13C NMR spectroscopy. *Carbohydr. Res.* **1994**, *253*, 1−12.
(51) Du, X.; Zhang, S.; Wang, L.; Wang, Y.; Fan, P.; Jia, W.; Zhang, P.; Huang, S. Single-Molecule Interconversion between Chiral Configurations of Boronate Esters Observed in a Nanoreactor. *ACS Nano* **2023**, *17* (3), 2881−2892.
(52) Wu, H.; Li, X.; Ji, H.; Svensson, B.; Bai, Y. Improved production of gamma-cyclodextrin from high-concentrated starch using enzyme pretreatment under swelling condition. *Carbohydr. Polym.* **2022**, *284*, No. 119124.
(53) Seung, D. Amylose in starch: towards an understanding of biosynthesis, structure and function. *New Phytol.* **2020**, *228* (5), 1490−1504.
(54) Li, H.; Yang, S.; Saravanamurugan, S.; Riisager, A. Glucose Isomerization by Enzymes and Chemo-catalysts: Status and Current Advances. *ACS Catal.* **2017**, *7* (4), 3010−3029.
(55) Carraher, J. M.; Fleitman, C. N.; Tessonnier, J.-P. Kinetic and Mechanistic Study of Glucose Isomerization Using Homogeneous Organic Brønsted Base Catalysts in Water. *ACS Catal.* **2015**, *5* (6), 3162−3173.
(56) Kimura, H.; Nakahara, M.; Matubayasi, N. In Situ Kinetic Study on Hydrothermal Transformation of d-Glucose into 5-Hydroxymethylfurfural through d-Fructose with 13C NMR. *J. Phys. Chem. A* **2011**, *115* (48), 14013−14021.
(57) Dias, F. F.; Panchal, D. C. Maltulose Formation During Saccharification of Starch. *Starch* **1987**, *39* (2), 64−66.
(58) Kobayashi, T.; Watanabe, Y.; Khuwijitjaru, P.; Adachi, S. Isomerization of maltose to maltulose under microwave heating using uncalcined scallop shell powder. *Food Bioprod. Process.* **2024**, *147*, 140−147.

https://doi.org/10.1021/acs.nanolett.5c04591
Nano Lett. 2026, 26, 74−82